Time Accurate Simulation of Nonequilibrium Flow inside the NASA Ames Electric Arc Shock Tube

Khalil Bensassi,* Aaron M. Brandis,†
AMA, Inc. at NASA Ames Research Center

Numerical investigations of the flowfield inside NASA Ames' Electric Arc Shock Tube have been performed. The focus is to simulate the experiments designed to reproduce shock layer radiation layer relevant to Earth re-entry conditions. This paper assess the current computational capability in simulating unsteady nonequilibrium flows in the presence of strong shock waves with state-of-the-art physical models. The technical approach is described with preliminary results presented for one specific flow condition. The numerical problems encountered during the computation of these flows are detailed, along with the methods used to resolve them. Post-shock conditions are discussed and compared to CEA equilibrium prediction.

I. Introduction

During the last twenty years, there has been a major increase in computational resources, thus massively parallel algorithms have been developed together with accurate physical models. Computational Fluid Dynamics (CFD) codes have become a major tool to study and predict real flight data over the whole (re)-entry trajectory of the space vehicle and hence to improve the design of spacecraft. Furthermore, computational tools are used to support wind tunnel data analysis.[1–3] This coupling between numerical simulations and hypersonic wind tunnel experiments is necessary because the two approaches are complementary, as the data from one are used to improve the other. Numerical simulations are used to provide a better understanding of the gas dynamic processes inside hypersonic test facilities and to supplement experimental knowledge. They are also used to improve the design of the experiments or to improve the tunnel operation characteristics and to compensate for the lack of information that cannot be directly measured in wind tunnels. Furthermore, experimental data are an important aspect of the validation process of the physical models and numerical methods used in CFD codes.

Shock tubes, such as the NASA Ames' Electric Arc Shock Tube (EAST),[4,5] present several computational challenges[6] because multiple aspects of the tunnel operation need to be taken into account. Modeling the entire facility from the arc-driver to the test section involves a large number of different physical processes, some of which are not well understood and/or are very complex. The arc-heating process in the driver gas requires an accurate description of the current distribution, therefore MHD equations need to be solved.[7] The diaphragm rupture would require an understanding of the material deformation up to the plasticity limit and then rupture propagation with some degree of non-uniformity. Diaphragm fragments, residual soot from previous experiments and wall ablation due to high wall temperatures may contaminate the flow. The hot jet of the driver gas penetrating into the cold driven tube is a three-dimensional problem and involves turbulent multi-scale mixing. Finally, radiative losses may need to be considered for certain conditions, which would require coupling the CFD code with a radiation solver.

On the numerical side, modeling the complete facility requires gridding a physical length of approximately eight meters. Crucial flow features such as shock and contact discontinuities (CD) need to be captured and resolved with good accuracy. Thus, the spacing, along the axial direction is then of the order of $10^{-5}-10^{-6}$ m. Furthermore, to resolve the boundary layers (BL) would require a grid spacing on the order of $10^{-6}-10^{-7}$ m in the radial direction. The stiffness is increased by the chemical and kinetics source terms governing the non-equilibrium processes. The modeling of the EAST facility is a multi-scale problem and a CFD tool that

*Research Scientist, Aerothermodynamics Branch. Senior Member AIAA. khalil.bensassi@nasa.gov
†Sr. Research Scientist, Aerothermodynamics Branch. Associate Fellow AIAA

accounts for all the physics, to our knowledge, does not exist yet. Therefore, in order to solve the problem, some assumptions need to be made to simplify the degree of detail. In the current work, the arc-heating process of the driver gas is not taken into account, The thermochemical state of the driver gas is considered in chemical and thermal equilibrium, at rest, and at a well defined constant temperature and pressure when the diaphragm breaks. The latter is considered ideal and thus providing a simple plane discontinuity between the driver and the driven gases during the first time step. The boundary layer is considered as laminar, and radiation cooling is not accounted for during the unsteady simulation. Despite these simplifications, EAST simulation remains very challenging and only a few attempts have been made in the past to tackle this formidable task. Kotov et al.[8] performed 1D and 2D time accurate simulations considering the gas in thermal equilibrium state, more recently Chandel et al.[9] are developing an innovative method based on shock frame velocity, with the main focus around the shock region and the test gas. Their method enables a drastic reduction -several order of magnitude- of the computational cost while maintaining a high resolution of the shock and the contact. In this work, we are interested in simulating the full shock tube, with the current state-of-the-art numerical methods and physical models used in modern aerothermodynamics solvers. The CFD tool that is used in this simulation is COOLFluiD[10,11] developed at the von Karman Institute, Belgium and was subject to many hypersonic flows validation for both steady and unsteady conditions.[12–16] The thermochemistry and the transport properties are provided by PLATO librery which develped at UIUC.

This paper is structured as follows. In Sections II, III, IV, V, we present the governing equations as well as the thermodynamics, kinetics and the transport properties. The related numerical discretization is described in Section VI. Herein, details of the flux evaluation, second-order reconstruction, implicit time integration scheme, and the related iterative solution for the non-linear system of equations is provided. In Section VII, we will discuss the results of the simulations. Finally, conclusion and a summary the remaining efforts to be performed are given in Section VIII.

II. Conservation equations

The equations governing multi-component reactive flows implemented in COOLFluiD[10,11] are derived from the kinetic theory of polyatomic reactive gas mixtures.[17–20] These equations can be split between conservation equations, thermochemistry, and transport fluxes. They are written in the following form:

$$\partial_t \rho_s + \boldsymbol{\partial_x} \cdot (\rho_s \boldsymbol{u}) + \boldsymbol{\partial_x} \cdot \boldsymbol{\mathcal{F}_s} = \dot{\omega}_s \qquad s \in \mathcal{S}, \tag{1}$$

$$\partial_t (\rho \boldsymbol{u}) + \boldsymbol{\partial_x} \cdot (\rho \boldsymbol{u} \otimes \boldsymbol{u} + p\boldsymbol{I}) + \boldsymbol{\partial_x} \cdot \boldsymbol{\Pi} = \boldsymbol{0} \tag{2}$$

$$\partial_t (\mathcal{E}_{tr} + \mathcal{E}_{in} + \tfrac{1}{2}\rho \boldsymbol{u}\cdot\boldsymbol{u}) + \boldsymbol{\partial_x} \cdot (\mathcal{E}_{tr} + \mathcal{E}_{in} + \tfrac{1}{2}\rho \boldsymbol{u}\cdot\boldsymbol{u} + p)\boldsymbol{u}) + \boldsymbol{\partial_x} \cdot (\boldsymbol{\Pi}\cdot\boldsymbol{u} + \boldsymbol{\mathcal{Q}}_{tr} + \boldsymbol{\mathcal{Q}}_{in}) = \boldsymbol{0} \tag{3}$$

$$\partial_t (\mathcal{E}_{in}) + \boldsymbol{\partial_x} \cdot (\boldsymbol{u}\mathcal{E}_{in}) + \boldsymbol{\partial_x} \cdot (\boldsymbol{\mathcal{Q}}_{in}) = \omega_{in} \tag{4}$$

where ∂_t denotes the time derivative, $\boldsymbol{\partial_x}$ the space derivative operator, ρ_s the mass density of the s^{th} species, , $\mathcal{S} = 1, ..., n_s$ the set of species indices, $n_s \geq 1$ the number of species, $\boldsymbol{u}$ the mass average flow velocity, $\boldsymbol{\mathcal{F}}_s$, $s \in \mathcal{S}$, the diffusion flux of the s^{th} species, $\dot{\omega}_s$, $s \in \mathcal{S}$, the production rate of the s^{th} species, $\rho = \sum_{s\in\mathcal{S}} \rho_s$ the total mass density, p the pressure, $\boldsymbol{\Pi}$ the viscous tensor, $\mathcal{E}_{tr}$ the internal energy per unit volume, $\mathcal{E}_{in}$ the translational energy per unit volume and $\boldsymbol{Q}_{tr}$ the translational component of the heat flux, $\boldsymbol{Q}_{in}$ the internal component of the heat flux. These equations have to be completed by the relations expressing the thermodynamic properties like p, $\mathcal{E}_{tr}$, $\mathcal{E}_{in}$, $\dot{\omega}_s$ the chemical production rates , $s \in \mathcal{S}$, ω_{in} the rate of internal energy exchange, and the transport fluxes $\boldsymbol{\mathcal{F}}_s$, $\boldsymbol{\Pi}$, $\boldsymbol{Q}_{tr}$ and $\boldsymbol{Q}_{in}$.

III. Thermodynamics

Thermodynamic properties of individual species are computed based on semi-classical statistical mechanics and using quantized energy levels and Boltzmann statistics. In the current work, these energy modes are considered decoupled, despite the quantum illegitimacy of this separation.[21] For molecules, these energies are translational, rotational, vibrational and electronic; and for atoms, translational and electronic modes. Rotational and vibrational energies are computed according to the rigid rotor and harmonic oscillator models respectively. Spectroscopic constants used to compute the thermodynamic properties are taken from Gurvich.[22] Statistical derivation of thermodynamic properties is given in Mayer.[23] Two-temperatures Park's model[24] is used. The pressure, p, the internal energy of translational origin per unit volume, $\mathcal{E}_{tr}$, and the

internal energy of internal origin per unit volume, $\mathcal{E}_{in}$ are in the form:

$$p = \sum_{i\in\mathcal{S}, i\neq e} \rho_s r_s T + \rho_e r_e T_{in}, \qquad \mathcal{E}_{tr} = \textstyle\sum_{i\in\mathcal{S}} \rho_s e_{tr,s}, \qquad \mathcal{E}_{in} = \sum_{i\in\mathcal{S}} \rho_s e_{in,s} \tag{5}$$

where $r_s = R/m_s$, R is the gas constant and m_s, $s \in \mathcal{S}$, mass os the s^{th} species, $e_{tr,s}$, $s \in \mathcal{S}$, is the sum of translational and rotational energies per unit mass at temperature T and $e_{in,s}$, $s \in \mathcal{S}$ is the sum of the vibrational and electronic energies at T_{in}.

IV. Transport properties

The Chapman-Enskog[20,25,26] method for the solution of the Boltzmann equations gives the transport fluxes $\mathbf{\Pi}$, $\boldsymbol{\mathcal{F}_s}, s \in \mathcal{S}, \boldsymbol{\mathcal{Q}}_{tr}$ and $\boldsymbol{\mathcal{Q}}_{in}$ as function of the macroscopic variables. The method can be extended to gases with discrete internal energy levels using multi-scale analysis of the Boltzmann equation.[18,27,28]

Transport flux expressions can be written in the form

$$\mathbf{\Pi} = p_{rel} - \kappa(\boldsymbol{\partial_x} \cdot \boldsymbol{u})\boldsymbol{I} - \eta(\boldsymbol{\partial_x u} + \boldsymbol{\partial_x u}^t - \tfrac{2}{3}(\boldsymbol{\partial_x} \cdot \boldsymbol{u})\boldsymbol{I}), \tag{6}$$

$$\boldsymbol{\mathcal{F}}_s = -\textstyle\sum_{m\in\mathcal{S}} C_{sm}\boldsymbol{d}_m - \rho Y_s\theta_s\boldsymbol{\partial_x} log T - \rho Y_s\theta_{s,in}\boldsymbol{\partial_x} log T_{in}, \qquad s \in \mathcal{S} \tag{7}$$

$$\boldsymbol{\mathcal{Q}}_{tr} = \textstyle\sum_{s\in\mathcal{S}} h_s\boldsymbol{\mathcal{F}}_s - \lambda_{tr}\boldsymbol{\partial_x} T - p\sum_{s\in\mathcal{S}} \theta_s\boldsymbol{d}_s \tag{8}$$

$$\boldsymbol{\mathcal{Q}}_{in} = \textstyle\sum_{s\in\mathcal{S}} e_{s,in}\boldsymbol{\mathcal{F}}_s - \lambda_{in}\boldsymbol{\partial_x} T_{in} - p\dfrac{T_{in}}{T}\sum_{s\in\mathcal{S}} \theta_{s,in}\boldsymbol{d}_s \tag{9}$$

with

$$\boldsymbol{d}_s = \frac{\boldsymbol{\partial_x} p_s}{p}, \qquad s \in \mathcal{S}, \tag{10}$$

$$\tag{11}$$

where p_{rel} denotes the relaxation pressure, κ the volume viscosity, η the shear viscosity, $\boldsymbol{I}$ the three dimensional identity tensor, $C_{sm}, s, m \in \mathcal{S}$, the multi-component flux diffusion coefficients, $\boldsymbol{d}_s$, $s \in \mathcal{S}$, the species diffusion driving forces, θ_s, $s \in \mathcal{S}$, the species translational and rotational thermal diffusion coefficient, θ_{in}, $s \in \mathcal{S}$, internal thermal diffusion coefficients, λ_{tr}, λ_{in} the translational and partial thermal conductivity, and ^{t} the transposition operator. In the current work, the relaxation pressure, the Soret effect, that is, diffusion due to temperature gradient, Dufour effects, that is, diffusion due to concentration gradient are not considered because of the harmonic-oscillator assumption and the orthogonality of the polynomials used for the expansion functions. Although no reasonable justification is available, the volume viscosity is also neglected and we do feel guilty in doing so.[29–31] The mass diffusion fluxes are obtained by solving the Stefan-Maxwell equations under the constraint $\sum_{s\in\mathcal{S}} \mathcal{F}_s = 0$.

The multi-component transport coefficients, κ, η, λ_{tr}, λ_{in}, $C = (C_{sm})s, m \in \mathcal{S}$,$\theta_s$, $s \in \mathcal{S}$, are smooth functions of the state variables which are not explicitly given by the kinetic theory. These transport coefficients have important symmetry properties inherited from the underlying kinetic framework. Their evaluation requires solving a linear systems.[17,19,20] The latter is expressed in terms of bracket integrals which are evaluated by means of spectral method which uses Laguerre-Sonine polynomials as basis functions. The contribution of internal energy to the thermal conductivity is taken into account by means of the generalized Eucken's correction.[25]

V. Kinetic processes

The molar production rates are the Maxwellian rates obtained from the kinetic theory[19,20] when the chemical characteristic times are larger than the mean free times of the molecules and the characteristic times of internal energy relaxation. The mass production/destruction term $\dot{\omega}_s$ for chemical species with partial densities ρ_s is given as

$$\dot{\omega}_s = M_s \sum_{r=1}^{n_r} \left(\nu_{sr}^{''} - \nu_{sr}^{'}\right) * \left\{ \mathcal{K}_r^f \prod_{s=1}^{n_s} \left(\frac{\rho_s}{M_s}\right)^{\nu_{jr}^{'}} - \mathcal{K}_r^b \prod_{s=1}^{n_s} \left(\frac{\rho_s}{M_s}\right)^{\nu_{jr}^{''}} \right\}, \qquad s \in \mathcal{S}$$

where $\mathcal{K}_r^f$ and $\mathcal{K}_r^b$ are the forward and backward rate constants of the i^{th} reaction, respectively. The forward reaction rate coefficients $\mathcal{K}_r^f$ are approximated by using Arrhenius empirical relations based on Park.[32] The backward rate are based on the fundamental relation $\mathcal{K}_r^b = \mathcal{K}_r^f/\mathcal{K}_e^f$, where $\mathcal{K}_e^f$ is the equilibrium constant.

The internal energy exchange term, ω_{in} is given by

$$\omega_{in} = \omega_{vt} + \omega_{cv} + \omega_{et} + \omega_{ec}$$

where ω_{vt} is vibrational-translational energy exchange in molecule heavy-particle collisions, ω_{cv} the creation or destruction of vibrational energy in chemical reactions, ω_{et} elastic collisions of electrons with heavy-particles, ω_{ec} electron impact ionization. The first energy transfer terms, ω_{vt} is evaluated based on a Landau-Teller model,[33] and the relaxation time are computed by means of Millikan and White formula as proposed by Park.[32] The second term ω_{cv} is computed by using the non-preferential dissociation model of Candler et al.[34] Finally, ω_{et} and ω_{ec} are based on Park.[35,36]

VI. Numerical Technique

The governing equations described in Sec. II and expressed in their strong form, are a set of hyperbolic parabolic partial differential equations with stiff source terms. This set of conservation equations can be rewritten in a compact form which is suitable for space and time discretization

$$\partial_t(r\mathbf{Q}) + \sum_{i\in\mathcal{D}}(r\partial_i\mathbf{F}_i^c) + \sum_{i\in\mathcal{D}}(r\partial_i\mathbf{F}_i^d) = r\boldsymbol{S} \tag{12}$$

where r is used for the axisymmetric flow formulation,[37] $\mathbf{Q}$ is the conservative variable, ∂_i the spatial derivative operator in the i^{th} direction, $\mathcal{D} = \{1, ..., d\}$ the indexing set of spatial directions, $d \in \{1, 2\}$ the spatial dimension, $\mathbf{F_i^c}$ the convective flux in the i^{th} direction, $\mathbf{F_i^d}$ the dissipative flux in the i^{th} direction, and $\boldsymbol{S}$ the source term. The conservative variable vector $\mathbf{Q}$ is given by

$$\mathbf{Q} = \left(\rho_s, \rho u, \rho v, \mathcal{E}_{tr} + \mathcal{E}_{in} + \frac{1}{2}\rho\boldsymbol{u}\cdot\boldsymbol{u}, \mathcal{E}_{in}\right)^t \tag{13}$$

whereas the convective flux $\mathbf{F_i^c}$ in the i^{th} direction is given by

$$\mathbf{F}_i^c = \left(\rho_1 u_i, ..., \rho_n u_i, \rho u_1 u_i + \delta_{i1}p, \rho u_2 u_i + \delta_{i2}p, (\mathcal{E}_{tr} + \mathcal{E}_{in} + \frac{1}{2}\rho\boldsymbol{u}\cdot\boldsymbol{u} + p)u_i, \mathcal{E}_{in}u_i\right)^t \tag{14}$$

and $\mathbf{F}^d$ the diffusive fluxes in the i^{th} direction

$$\mathbf{F}_i^d = (\mathcal{F}_{1i}, ..., \mathcal{F}_{ni}, \Pi_{i1}, \Pi_{i2}, \mathcal{Q}_{tr,i} + \mathcal{Q}_{in,i} + \Pi_{i,1}u_1 + \Pi_{i,2}u_2)^t \tag{15}$$

and $\mathbf{S}$ is the source term

$$S = (\dot{\omega}_s, 0, \omega_{axi}, 0, \omega_{in})^t \tag{16}$$

where ω_{axi} is axisymmetric source term. The system of coupled partial differential equations, Eqs. 12, are discretized using the finite volume method.[38]

A. Space discretization

The convective fluxes are computed using the $AUSM_{UP}^+$ scheme.[39–41] In order to get second order accuracy, each one of the cell centered state variables u_i is linearly extrapolated to the face quadrature points as follows:

$$\tilde{u}(x_q) = u_i + \phi_i\nabla u_i.(x_q - x_i) \tag{17}$$

where x_i denotes the centroid position of the control volume Ω_i. The linearly reconstructed state variables $\tilde{u}$ are calculated using a least-squares method.[42] In order to prevent the appearance of oscillations near discontinuities, a flux limiter ϕ_i is needed for the reconstructed states. In the present work, Venkatakrishnan's limiter[43] is used.

B. Implicit Time integration

The second order time accurate Crank-Nicolson scheme is obtained by discretizing Eq. (12) in time. For a non-moving grid, Eq. (12) becomes

$$r_i \Omega_i \mathcal{T} \frac{\mathbf{P}_i^{n+1} - \mathbf{P}_i^n}{2\Delta t} = -\frac{1}{2}\left[\mathcal{R}_i\left(\mathbf{P}^{n+1}\right) + \mathcal{R}_i\left(\mathbf{P}^n\right)\right] \tag{18}$$

where $\mathcal{T}$ is a transformation matrix used for a change of variable, $\delta\mathbf{Q} = \frac{\partial \mathbf{Q}}{\partial \mathbf{P}}\delta\mathbf{P} = \mathcal{T}\delta\mathbf{P}$ between primitives, $\mathbf{P} = (\rho_s, u, v, T_{tr}, T_{in})^t$ and conservative, $\mathbf{Q}$ variables, $\mathcal{R}_i$ includes the convective fluxes, $\mathbf{F}_i^c$, diffusive fluxes, $\mathbf{F}_i^d$ and the source terms $\mathbf{S}_i$ belonging to the control volume Ω_i :
if we define a pseudo-residual $\mathcal{R}_i^*$ as

$$\mathcal{R}_i^*\left(\mathbf{P}^{n+1}\right) = r_i \Omega_i \mathcal{T} \frac{\mathbf{P}_i^{n+1} - \mathbf{P}_i^n}{\Delta t} + -\frac{1}{2}\left[\mathcal{R}_i\left(\mathbf{P}^{n+1}\right) + \mathcal{R}_i\left(\mathbf{P}^n\right)\right] \tag{19}$$

we obtain the fully implicit coupled non-linear equations

$$\mathcal{R}_i^*\left(\mathbf{P}^{n+1}\right) = 0. \tag{20}$$

which have to be solved at each time step by some approximate method. This non-linear system is similar to Eq. (20), which is solved using Newton's method at every time step.

C. Iterative solution for non-linear equations

The system Eq. (20), with unknowns $\mathbf{P}^{n+1}$, is solved using an iterative Newton procedure which is based on successive iterations, starting from an initial guess $\mathbf{s}^0$ and requiring the linearization of $\mathcal{R}^*$:

$$\mathcal{R}^*(\mathbf{s}) \simeq \mathcal{R}^*(\mathbf{s}^k) + \mathcal{J}(\mathbf{s}^k)\left(\mathbf{s} - \mathbf{s}^k\right). \tag{21}$$

Herein, $\mathcal{J}$ is the Jacobian matrix of the non-linear system which is given by:

$$\mathcal{J}(\mathbf{s}^k) = \left.\frac{\partial \mathcal{R}^*}{\partial \mathbf{s}}\right|_{\mathbf{s}=\mathbf{s}^k} = \left(\frac{\Omega}{\Delta t^n}\mathbf{I} - \frac{1}{2}\left.\frac{\partial \mathcal{R}^*}{\partial \mathbf{Q}}\right|_{\mathbf{Q}=\mathbf{s}^k}\right) \tag{22}$$

The resulting linear system and the update of the approximate solution can be expressed as:

$$\begin{cases} \mathcal{J}\left(\mathbf{s}^k\right)\Delta\mathbf{s}^k &= -\mathcal{R}^*(\mathbf{s}^k) \\ \mathbf{s}^{k+1} &= \mathbf{s}^k + \Delta\mathbf{s}^k \end{cases} \tag{23}$$

At each time step, this linear system Eq. (23) is solved implicitly until convergence using a Newton method. The latter requires a matrix inversion which is generally achieved by approximate methods. We use the Generalized Minimum RESidual (GMRES) algorithm, complemented with an Additive Schwartz pre-conditioner both provided by the PETSc library.[44,45]

VII. Results

Numerical simulation of the transient flow inside EAST facility has been performed using the total length of the tube, that is eight meters. Two-dimensional uniform grid was used for this simulation, the level of refinement was chosen according to,[6] with an axial spacing of $\Delta x = 10^{-3}m$, and a radial spacing with $10^{-6}m$ as a first-cell distance to the wall and a stretching factor of 1.1. The total number of gird in the driven part is 8400×128. Similar grid spacing was applied in the driven part, with a length of 0.1m. The wall is considered as isothermal at $T_w = 300K$ and no slip wall boundary conditions is applied. A symmetry conditions was applied on the boundary defined by $y = 0$, supersonic boundary condition at the end of the driven tube and slip wall at the end of the driver tube. Air was used as a test gas, the driver gas is composed of 99% of Helium and 1% Nitrogen. The initial conditions are given in Table 1.

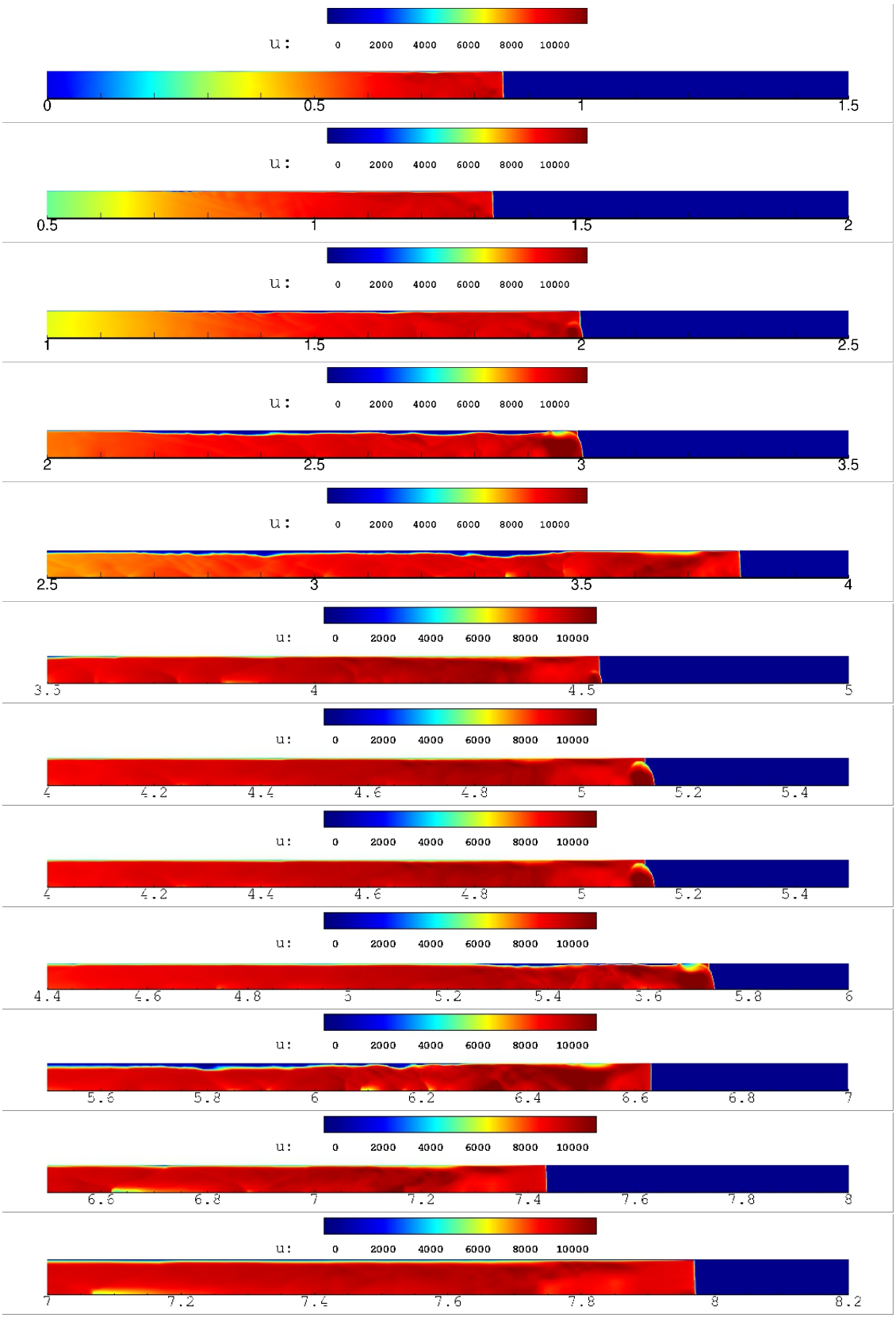

Figure 1. u-velocity flow field at different time step, m/s

	driver	driven
	Y_{N_2} : 0.0144	Y_{N_2} : 0.79
	Y_{He}: 0.9856	Y_{O_2} : 0.21
ρ, kg/m^3	1.10546	3.0964 x 10^{-4}
T, K	6000	300
p, Pa	12.7116 x 10^6	26.771

Table 1. Initial conditions at diaphragm rupture

The simulation was run until the shock arrives at the test-section located around 7.8 meters starting from the diaphragm position. Fig. 1 shows the x-velocity flow filed at different locations of shock.

As shown, there is a disturbance which is created on the symmetry axis at the shock position. This disturbance grows in time which makes the shock bends along the radial direction and starting from the symmetry axis. Once the disturbance reaches the wall, the shock becomes straight and continues its run. This disturbance appears twice, around 1.7 m and 4.2 m and last for about 2 m of shock traveling distance. The root of this disturbance has been investigated by performing two additional inviscid simulations with and without axisymmetric terms. The same conditions as the viscous simulation were used, and a uniform grid was applied in the radial direction -the boundary layer is not considered-. It was found that two-dimensional axisymmetric inviscid simulation exhibits shock bending while in pure two-dimensional -without axisymmetric terms- inviscid simulation, the shock bending did not show up. This first result tends to indicate that the axisymmetric source term may be the cause of this disturbances. Additional runs are needed in order to confirm this observation. In future work, we will consider the three-dimensional simulation of a 1/16 π-slice of the tube, where symmetry is enforced on the sides, thus avoiding the use of an axisymmetric source term.

The shock speed has been calculated by considering the shock arrival at a certain location as a 10% pressure rise with respect to the undisturbed region -initial test gas pressure-. Two fit strategies were applied using an exponential and a linear method. Fig. 2 shows the difference between the two methods and Tab. 2, gives the shock speed and the corresponding equilibrium temperature, which was calculated using CEA,[46] at different locations and for both curves fit methods.

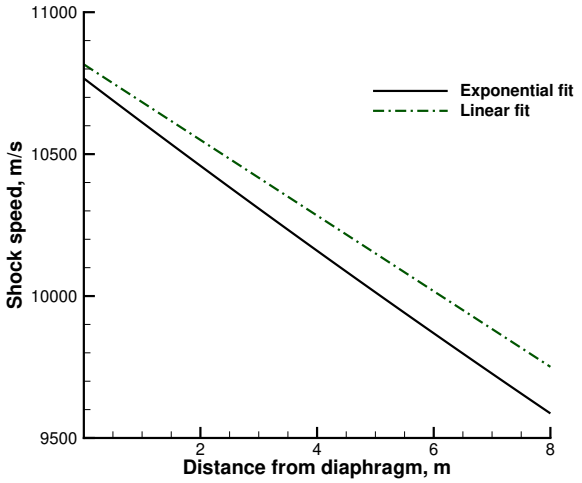

Figure 2. Shock velocity using linear and exponential fit , m/s

Even though there is a less than 2% difference between the two methods, both speeds will be used for the analysis of the post-shock conditions.

Fig. 3 shows translational and vibrational temperature profiles at different locations, and the equilibrium

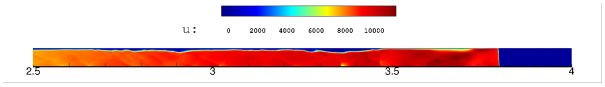

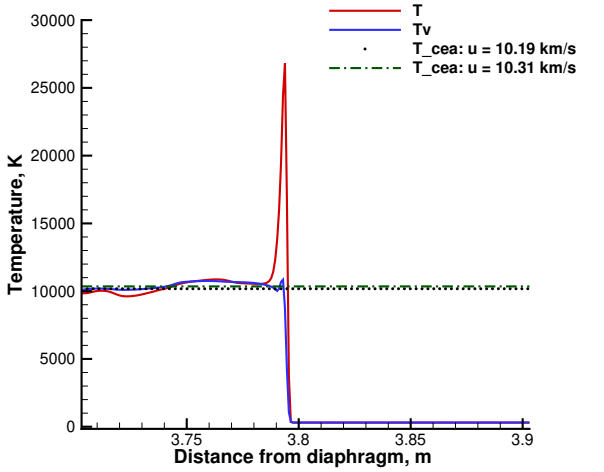

(a)

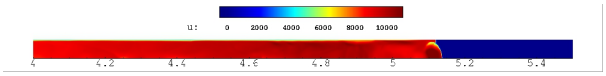

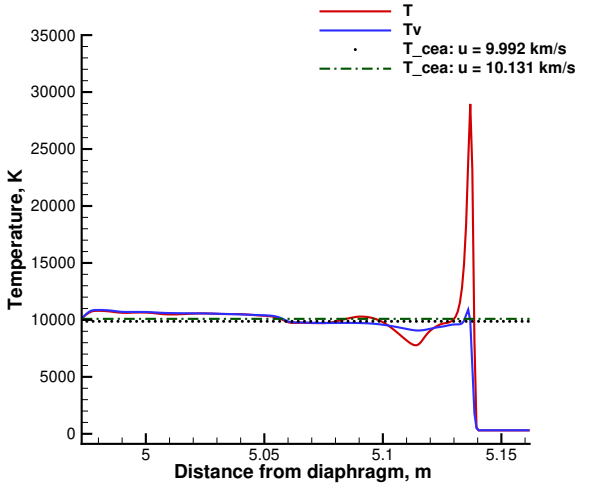

(b)

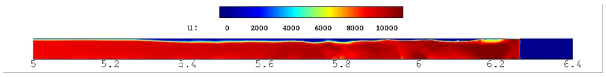

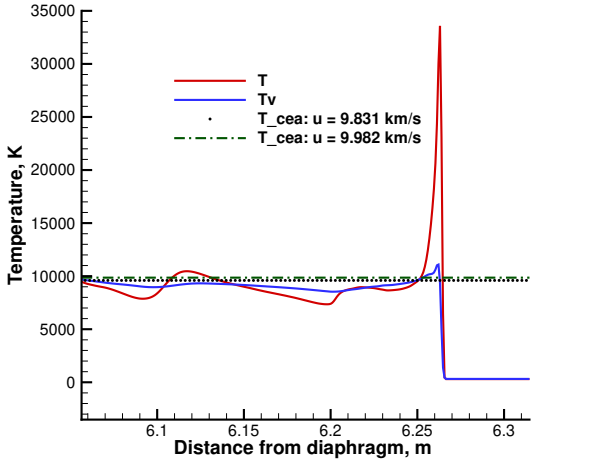

(c)

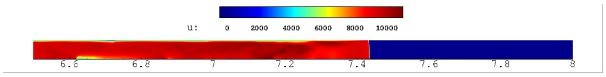

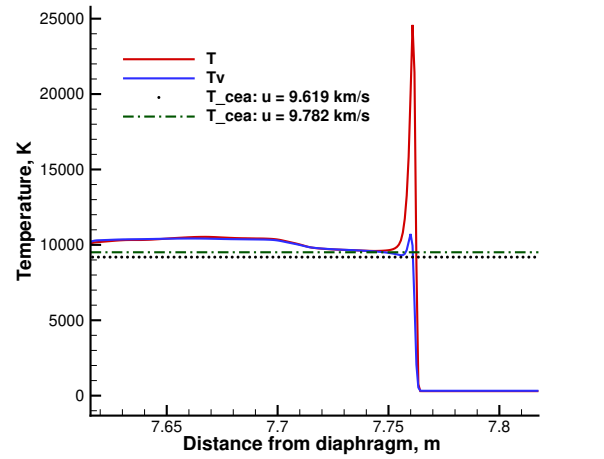

(d)

Figure 3. Translational and vibrational temperature centerline profiles at different shock location

Position, m	3.79	5.14	6.26	7.76
Shock Speed -exp fit-, km/s	10.189	9.992	9.831	9.619
$T^{cea}_{equilibiurm}$, K	10180	9875	9599	9188
Shock Speed -lin fit-, km/s	10.310	10.131	9.982	9.782
$T^{cea}_{equilibiurm}$, K	10352	10093	9859	9509

Table 2. Shock speed at different location from diaphragm

temperature predicted by CEA for two shock speeds - obtained using exponential and linear fits-. These profiles are centered around the shock position and also include a 10 cm post-shock region. Figs. 3(a), 3(b), 3(c) ,3(d) show that both the peak translational temperature and the profiles in the post-shock region are different. The maximum translational temperature is changing due to shock bending. The latter initiates a compression region resulting in an increase of the post-shock translational temperature peak. This unsteadiness of the flow can be seen in the post-shock region, where the centerline profiles of translational and vibrational temperature are affected by the interaction of the disturbance and the wall.

VIII. Conclusions

Time accurate simulation of thermo-chemical nonequilibrium flow inside EAST facility was performed using a two-dimensional second-order axisymmetric finite volume solver. Although the present work is a premiere as second order time implicit nonequilibrium simulation of the complete EAST facility, the initial goal was to assess the capabilities of the current state-of-the-art models in addressing unsteady flows with stiff source terms. It was found that the axisymmetric source term generates a numerical instability that appears as shock bending. This instability is time dependent which greatly affects the shock speed. The latter was calculated, in a post-processing step, with two curves fit methods. The obtained shock speed was used to compute equilibrium conditions predicted by CEA. Translational and vibrational temperatures profiles were compared to CEA equilibrium prediction. Good agreement was obtained with CEA prediction close to the test-section -shock location is at 7.6 m from the diaphragm- and just behind the shock, fully equilibrium is not retrieved due to the deceleration of the shock.

In future work, three-dimensional simulation - in axisymmetric mode- will be performed, which we believe will alleviate the instability problem of the axisymmetric source term. Also, the current axial grid resolution is not enough in order to capture the correct waves speeds, and an optimal grid would have a higher resolution only in the region of interest i.e 20 cm behind the shock, thus r-adaptation will be explored.

References

[1]Nompelis, I., *Computational Study of Hypersonic Double-Cone Experiments for Code Validation*, Ph.D. thesis, University of Minnesota, May 2004.

[2]Bensassi, K., *Contribution to the Numerical Modeling of the VKI Longshot Hypersonic Wind Tunnel*, ISBN 978-2-87516-072-0, von Karman Institute for Fluid Dynamics, 2014.

[3]Goozee, R. J., *Simulation of a Complete Shock Tunnel Using Parallel Computer Codes*, Ph.D. thesis, Division of Mechanical Engineering, University of Queensland, 2003.

[4]Cruden, B., Martinez, R., Grinstead, J., and Olejniczak, J., "Simultaneous Vacuum-Ultraviolet Through Near-IR Absolute Radiation Measurement with Spatiotemporal Resolution in An Electric Arc Shock Tube," *41st AIAA Thermophysics Conference*, edited by AIAA-2009-4240, San Antonio, Texas, 2009.

[5]Cruden, B., "Absolute Radiation Measurements in Earth and Mars Entry Condition," *Radiation and Gas-Surface Interaction Phenomena in High-Speed Re-Entry*, Von Karman Institute Lecture Series, 2014.

[6]Kotov, D. V., Yee, H., Panesi, M., Prabhu, D. K., and Wray, A. A., "Computational challenges for simulations related to the NASA electric arc shock tube (EAST) experiments," *Journal of Computational Physics*, Vol. 269, No. Supplement C, 2014, pp. 215 – 233.

[7]Sharma, S. and Park, P., "Operating characteristics of a 60- and 10-cm electric arc-driven shock tube. I - The driver. II - The driven section," *Journal of Thermophysics and Heat Transfer*, Vol. 4, No. 3, 1990, pp. 259–265.

[8]Kotov, D. V., Yee, H. C., Panesi, M., Prabhu, D., and Wray, A., "1D and 2D simulations for the NASA Electric Arc Shock Tube experiments," *Annual Research Briefs*, Center for Turbulence Research, 2012.

[9]Chandel, D., Nompelis, I., and Candler, G. V., "Computations of High Enthalpy Shock-waves in Electric Arc Shock-Tube (EAST) at NASA Ames," *2018 AIAA Aerospace Sciences Meeting*, American Institute of Aeronautics and Astronautics, 2018.

[10]Lani, A., Quintino, T., Kimpe, D., and Deconinck, H., "The COOLFluiD Framework - Design Solutions for High-Performance Object Oriented Scientific Computing Software," *International Conference Computational Science 2005*, Vol. 1, Springer-Verlag, Atlanta, 2005, pp. 281–286.

[11]Lani, A., Quintino, T., Kimpe, D., Deconinck, H., Vandewalle, S., and Poedts, S., "The COOLFluiD Framework: Design Solutions for High-Performance Object Oriented Scientific Computing Software," *Computational Science ICCS 2005*, edited by P. M. A. S. V. S. Sunderan, G. D. van Albada and J. J. Dongarra, Vol. 1 of *LNCS 3514*, Emory University, Springer, Atlanta, GA, USA, May 2005, pp. 281–286.

[12]Panesi, M., Lani, A., Magin, T., Pinna, F., Chazot, O., and Deconinck, H., "Numerical investigation of the non equilibrium shock-layer around the EXPERT vehicle," *AIAA Paper 2007-4317*, 38th AIAA Plasmadynamics and Lasers Conference, Miami (Florida), Jun 2007.

[13]Bensassi, K., Lani, A., Rambaud, P., and Chazot, O., "Numerical Simulation of Hypersonic Flow in VKI-Longshot Contoured Nozzle," *40th Fluid Dynamics Conference and Exhibit*, No. AIAA-4857, American Institute of Aeronautics and Astronautics, 2010.

[14]Bensassi, K., Lani, A., and Rambaud, P., "Numerical Investigations of Local Correlation-Based Transition Model in Hypersonic Flows," *42nd AIAA Fluid Dynamics Conference and Exhibit*, No. AIAA3151, American Institute of Aeronautics and Astronautics, 2012.

[15]Bensassi, K., Lani, A., Chazot, O., and Rambaud, P., "Arbitrary Lagrangian Eulerian Simulation of a Moving Piston in Hypersonic Ground Test Facility," *42nd AIAA Fluid Dynamics Conference and Exhibit*, No. AIAA-3265, American Institute of Aeronautics and Astronautics, 2012.

[16]Bensassi, K., Lani, A., and Rambaud, P., "Unsteady simulation of hypersonic flow around a heat flux probe in ground testing conditions," *International Journal of Heat and Mass Transfer*, Vol. 113, 2017, pp. 889 – 897.

[17]Hirschfelder, J. O., Curtiss, C. F., and Bird, R. B., *Molecular theory of gases and liquids*, John Wiley and Sons, New York, 1967.

[18]Nagnibeda, E. and Kustova, E., *Non-Equilibrium Reacting Gas Flows: Kinetic Theory of Transport and Relaxation Processes*, Heat and Mass Transfer, Springer Berlin Heidelberg, 2009.

[19]Ern, A. and Giovangigli, V., *Multicomponent Transport Algorithms,*, Vol. 24, Lecture Notes in Physics, New Series, Monographs, 1994.

[20]Giovangigli, V., *Multicomponent flow modeling*, Birkhäuser, 1999.

[21]Giordano, D., "Impact of the Born-Oppenheimer Approximation on Aerothermodynamics," *Journal of Thermophysics and Heat Transfer*, Vol. 21, No. 3, 2007, pp. 647–657.

[22]Gurvich, L. V., Veits, I. V., and Alcock, C. B., *Thermodynamic Properties of Individual Substances*, New York, Hemisphere Publishing Corp., 1989, 1989.

[23]Mayer, J. and Mayer., M., *Statistical mechanics*, Wiley, New York, 1946.

[24]Park, C., *Nonequilibrium Hypersonic Aerothermodynamics*, John Wiley and Sons, New York, 1989.

[25]Chapman, S. and Cowling, T., *The Mathematical Theory of Non-Uniform Gases*, Cambridge University Press, London, U.K., 1970.

[26]Ferziger, J. H. and Kaper, H. G., *Mathematical theory of transport processes in gases*, North-Holland Publishing Company, Amsterdam–London, 1972.

[27]Ern, A. and Giovangigli, V., "Kinetic theory of dilute gas mixtures with independent internal energy modes near equilibrium," *Physica A: Statistical Mechanics and its Applications*, Vol. 224, No. 3, 1996, pp. 613 – 625.

[28]Magin, T. E., Graille, B., and Massot, M., "Hydrodynamic model for molecular gases in thermal nonequilibrium," *AIP Conference Proceedings*, Vol. 1501, No. 1, 2012, pp. 231–238.

[29]Emanuel, G., "Effect of bulk viscosity on a hypersonic boundary layer," *Physics of Fluids / Volume 4 / Issue 3*, , No. 491, 1991.

[30]Bruno, D., Esposito, F., and Giovangigli, V., "Relaxation of rotational-vibrational energy and volume viscosity in H-H2 mixtures," *J Chem Phys*, Vol. 8, No. 138, 2013.

[31]Ern, A. and Giovangigli, V., "Volume viscosity of dilute polyatomic gas mixtures." *Eur. J. Mech. B/Fluids*, Vol. 14(5):653–669,, 1995.

[32]Park, C., "Review of chemical-kinetic problems of future NASA missions. I - Earth entries," *Journal of Thermophysics and Heat Transfer*, Vol. 7, No. 3, 2018/11/22 1993, pp. 385–398.

[33]Landau, L. and Teller, E., "Theory of Sound Dispertion," *Physikalische Zeitschrift der Sowjetunion*, Vol. 10, No. 34, 1936.

[34]Candler, G. V. and MacCormack, R. W., "Computation of weakly ionized hypersonic flows in thermochemical nonequilibrium," *Journal of Thermophysics and Heat Transfer*, Vol. 5, No. 3, 2018/11/22 1991, pp. 266–273.

[35]Park, C., "Assessment of Two-Temperature Kinetic Model for Ionizing Air," *AIAA*, June 1987, pp. AIAA 87–1574,.

[36]Gnoffo, P. A., Gupta, R. N., and Shinn, J. L., "Conservation equations and physical models for hypersonic air flows in thermal and chemical non-equilibrium." Technical Paper 2867, NASA, 1989.

[37]Broglia, R., Manna, M., Deconinck, H., and Degrez, G., "Development and validation of an axisymmetric solver for hypersonic flows," VKI TN 188, von Karman Institute for Fluid Dynamics, St.-Genesius-Rode, Belgium, May 1995.

[38]Barth, T. and Ohlberger, M., "Finite Volume Methods: Foundation and Analysis," *Encyclopedia of Computational Mechanics*, edited by L. John Wiley & Sons, 2004.

[39]Liou, M. S. and Steffen, C. J. J., "A new flux splitting scheme," *Journal of Computational Physics*, Vol. 107, 1993, pp. 23–39.

[40]Liou, M. S., "A sequel to AUSM: AUSM+," *Journal of Computational Physics*, Vol. 129, 1996, pp. 363–382.

[41]Liou, M. S., "A Further Development of the AUSM$^+$ Scheme Towards Robust and Accurate Solutions for All Speeds," *16th AIAA Computational Fluid Dynamics Conference*, Orlando, Florida, June 2003, AIAA 2003-4116.

[42]Barth, T., "Aspects of unstructured grids and finite volume solvers for the Euler and Navier-Stokes equations," 25th Computational Fluid Dynamics Lecture Series, Von Karman Institute, March 1994.

[43]Venkateswaran, S. and Merkle, C. L., "Analysis of preconditioning methods for the Euler and Navier-Stokes equations," VKI LS 1999-03, von Karman Institute for Fluid Dynamics, St.-Genesius-Rode, Belgium, March 1999.

[44]Balay, S., Gropp, W. D., McInnes, L. C., and Smith, B. F., *Efficient Management of Parallelism in Object-Oriented Numerical Software Libraries*, chap. 8, Birkhäuser, 1997, pp. 163–202.

[45]Laboratory, A. N., "PETSc: Portable, Extensible Toolkit for Scientific Computation," 2007.

[46]Snyder, C. A., "Chemical Equilibrium with Applications," .